PHYSICAL REVIEW B **102**, 035446 (2020)

First-principles calculations of the electronic structure and magnetism of nanostructured $CoFe_2O_4$ microgranules and nanoparticles

Sumayya M. Ansari,[1] Vikas Kashid,[2] Hemant Salunke,[3] Debasis Sen,[4,5] Yesh D. Kolekar,[1,*] and C. V. Ramana[6,†]
[1]*Department of Physics, Savitribai Phule Pune University, Pune-411007, India*
[2]*Peter Grünberg Institut and Institute for Advanced Simulation, Forschungszentrum Jülich & JARA 52428 Jülich, Germany*
[3]*Technical Physics Division, Bhabha Atomic Research Centre, Mumbai-400 085, India*
[4]*Solid State Physics Division, Bhabha Atomic Research Centre, Mumbai-400 085, India*
[5]*Homi Bhabha National Institute, Anushaktinagar, Mumbai-400 094, India*
[6]*Center for Advanced Materials Research (CMR), University of Texas at El Paso, El Paso, Texas 79968, USA*

(Received 18 June 2018; revised 17 December 2019; accepted 6 February 2020; published 30 July 2020)

A detailed study of the structural and magnetic properties of inverse spinel $CoFe_2O_4$ nanoparticles and nanostructured $CoFe_2O_4$ microgranules is made by the first-principles calculations. We have estimated the relative strengths of crystal fields, exchange fields, and magnetic exchange interactions using the electronic structure calculations and electron density maps. We find that the electron-electron correlation plays a significant role in obtaining the correct ground-state structure. A significant local structural distortion at the octahedral site and "inverted" sublattice occupancy in $CoFe_2O_4$ affects the magnetic exchange interactions substantially. The trends in magnetic exchange interactions are analyzed in terms of structural parameters and the features of their electronic structures and magnetic properties. We find that Fe states in $CoFe_2O_4$ are extremely localized, irrespective of the symmetry of the site. Also, Co and Fe ions prefer their high-spin configurations with higher spin moments at octahedral sites.

DOI: 10.1103/PhysRevB.102.035446

I. INTRODUCTION

Spinel oxides, AB_2O_4, have been the subject of continuously evolving scientific research, as they constitute a fascinating class of materials with a plethora of interesting electrical, thermal, and magnetic properties. In addition, spinel oxides are ideal materials for investigating structure-property relationships and, subsequently, engineering their functional properties for device applications. Properties of the spinel oxide structure are significantly affected by the actual distribution of the cations A and B. The cation disorder or distribution is primarily determined by the method of material preparation [1], heat treatment process, and chemical environment [2–4]. For example, the manganese ferrite bulk material was present in a mixture of normal and inverse spinel structure with the range of around 20% between normal and inverse spinel structure [5]. The cation disorder of 80% in cobalt ferrite structure has been investigated at high temperatures up to 870 K [6] and 75% at 1170 K after annealing the powder sample [7]. The degree of cation disorder can be distinctly characterized by the so-called degree of inversion x, which is defined as the fraction of divalent metal cations in octahedral sites as $[A_{1-x}B_x]_{\mathrm{Tet}}\{A_xB_{2-x}\}_{\mathrm{Oct}}O_4$ where x can take values between 0 and 1. The "normal spinel" compounds are those with $x = 0$ when the A cations in AB_2O_4 occupy the tetrahedral sites and the B cations occupy the octahedral sites. The "inverse spinel" compounds are those with $x = 1$, where the tetrahedral sites are completely occupied by the B cations, while the octahedral sites are occupied by the equal amounts of A and B cations.

A fundamental, scientific understanding of the degree of cation disorder and the interplay between the cation distribution and fundamental properties is very important in spinel compounds. It has been established, based on the numerous studies on a variety of spinels, that the electronic [8] and thermal [9,10] properties can be controlled by manipulating the degree of cation disorder. Recently, magnetic spinels with different magnetic constituents at A and B sublattices have gained prominence as they widen the scope of functionalities of spinel oxides due to the presence of different magnetic interactions. Moreover, magnetism offers greater perspectives regarding coupling between various degrees of freedom, such as the lattice and the magnetic ones [11,12]. Here, the specific spinel oxide of our interest is cobalt ferrite ($CoFe_2O_4$, CFO), which is quite important for numerous scientific and technological applications due to its high bulk anisotropy constant and reasonably large magnetization values [13–15]. Surface characteristics affect nanoscale CFO integration into applications because the magnetic behavior of CFO deviates from bulk properties due to surface spin disorder effects [16], surface anisotropy [17], and exchange biasing [18]. For the bulk lattice, CFO possesses an inverse cation distribution as $[Fe^{3+}]_T\{Co^{2+}Fe^{3+}\}_O O_4$, with Fe^{+3} cations occupying the A sites and Co^{+2} occupying B site. The accepted value for the cubic lattice parameter is 8.39 Å, although it varies slightly with the stoichiometry and method of preparation [19]. The deformation of oxygen lattice by displacements along a local

---

[*] Corresponding author: ydkolekar@gmail.com

[†] Corresponding author: rvchintalapalle@utep.edu

(111) direction is represented by the deviation of oxygen position parameter u from the value ($3/8$) which is appropriate for cubic close packing. The Fe^{+3} ($3d^5$; $t_{2g}{}^3 e^2{}_g$) has $S = 5/2$ and a spin moment of $5\mu_B$. Moreover, high-spin Co^{+2} ($3d^7$; $t_{2g}{}^5 e_g{}^2$) has $S = 3/2$ and a spin moment of 3 μ_B, but at the B site the cobalt can also have a significant unquenched orbital moment of ∼0.6 μ_B [20,21], which is responsible for strong cubic anisotropy $K_{c1} \approx 290\,\mathrm{kJ\,m^{-3}}$ along the (100) easy directions. Although the magnetic moment of an isolated Co^{+2} aligns along a local (111) trigonal axis [19], the resultant bulk anisotropy lies along the (100) plane [22]. The net magnetic moment of CFO is about 3.6 μ_B per formula, and the magnetization of the bulk sample is $455\,\mathrm{kA\,m^{-1}}$ or $86\,\mathrm{A\,m^2\,kg^{-1}}$ (86 emu/g), based on the x-ray density of $5290\,\mathrm{kg\,m^{-3}}$. Since the ferrimagnetic Néel temperature of CFO is ∼790 K, the ground-state, $T = 0$, values are slightly higher.

Theoretical studies [23–26] focused on the ideal inverse and normal spinels of CFO by the local spin density approximation (LSDA) [23] and beyond, for example, by invoking the on-site Coulomb repulsion energy (U) through the LSDA + U [24] and GGA + U (generalized gradient approximation + U) approaches [25] or using the self-interaction corrected (SIC)-LSDA method [26,27]. The LSDA approach usually describes these materials to be half-metallic or metallic, if no distortions are included. The transition-metal (TM) d states are poorly described by the conventional local density approximation (LDA) or generalized gradient approximations (GGA) based standard band theory, which resulted in bringing the states close to Fermi energy [28]. The strongly correlated d bands are correctly described using extended density functional theory with a Hubbard U parameter for on-site Coulomb interaction. CFO has been identified as nonmetallic within the DFT+U approach [28,29]. Although self-interaction corrections also provide a better description to the strongly correlated d electrons, the methods are computationally expensive [30]. Besides the theoretical studies for bulk normal and inverse spinel CFO structures [23,29], Fritsch and Ederer [31] and Hou *et al.* [28] have investigated the cation distribution in CFO at certain degrees of inversion. Recently, a few combined experimental and theoretical attempts were made to investigate CFO in its thin-film form or in powder form [13,21,32–38]. The experimental efforts were directed mostly on the synthesis, characterization, and applications of CFO in biomedical, magnetostrictive, and spintronics [39–44]. Theoretical investigations by Caffrey *et al.* predicted CFO as a suitable barrier for spin filtering applications in devices [27]. In nanoscale and bulk form, superparamagnetism, surface anisotropy, and noncollinear (canted) spin structures are the most relevant effects associated with CFO nanoparticles (NPs) [39–44]. Some of the studies reported diverse magnetic behavior of CFO NPs—bulk and thin/thick films with respect to size, shape, composition, and synthesis methods [45–48]. However, detailed theoretical insights into the effects of surface characteristics on the magnetic properties of CFO requires further study.

In the present work, we have made an attempt to elucidate the fundamental aspects of electronic structure and magnetism of CFO with variable size, specifically, CFO NPs (denoted as CF1) and nanostructured CFO microgranules (denoted as CF2). The primary objective of the study is elucidating the effect of size on structural parameters, electronic structure, magnetic properties, and the crystal and exchange field splitting. We have performed calculations based on the density functional theory (DFT) with a GGA+U approach and investigated the electronic and magnetic properties of CFO with various degrees of inversion. Our results indicate that with the variation of degree of inversion in CFO, the crystal-field splitting as well as exchange splitting at tetrahedral and octahedral sites are affected. Our results show that the Co ions strongly prefer octahedral sites. The presence of Co ions at tetrahedral sites, due to temperature effects, like to be far away from the Co at octahedral sites. Also, the Co and Fe ions always prefer the high-spin configurations in the studied normal, inverse, and partial inverse spinel CFO.

II. COMPUTATIONAL DETAILS

The electronic structure calculations were performed for inverse spinel CFO structures using DFT as implemented in the Vienna *Ab Initio* Simulation Package (VASP) [49]. To determine the ground-state energy, we considered the ferrimagnetic as well as antiferromagnetic magnetic structures, where the spins at A and B sublattices are aligned in a parallel and

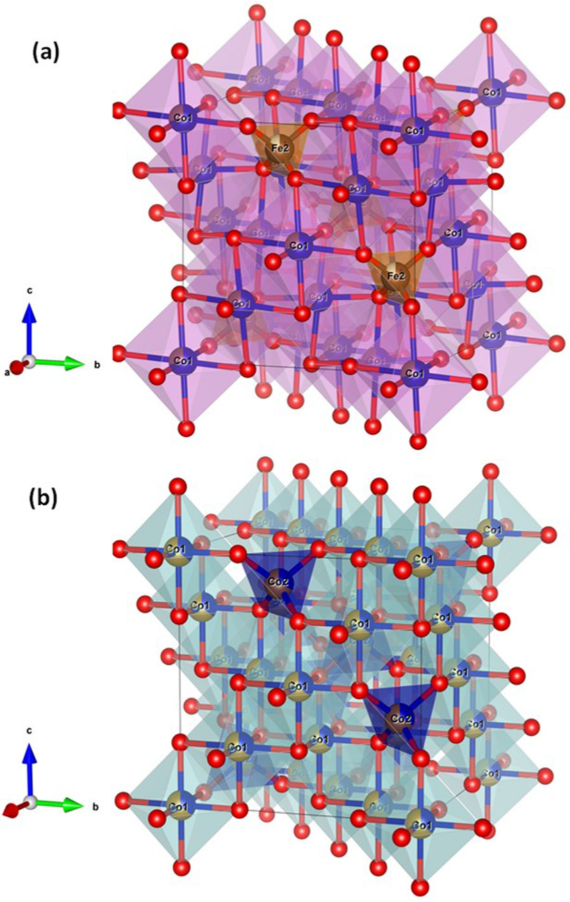

FIG. 1. The crystal structure of CF1 (a), where octahedral, tetrahedral, and oxygen atoms are shaded in pink, brown, and red, respectively, and the crystal structure of CF2 (b), where octahedral, tetrahedral, and oxygen atoms are shaded in sky blue, blue, and red, respectively.

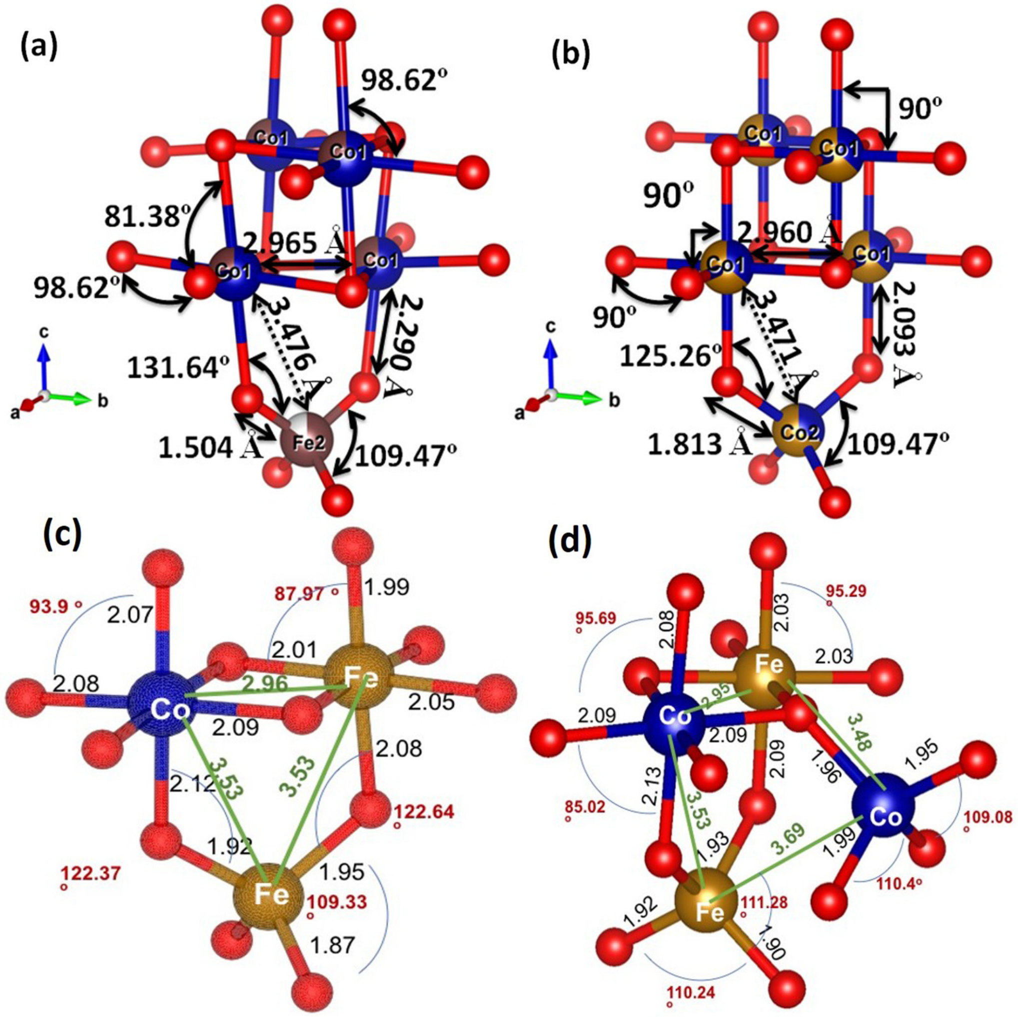

FIG. 2. The neighborhood around the tetrahedral and octahedral sites in CF1 (a) and CF2 (b) along with bond angles and bond lengths. The calculated bond lengths and bond angles obtained from first-principles calculations are shown for (c) CF1 and (d) CF2 structures.

antiparallel manner, respectively. The plane-wave cutoff for the basis functions was set to 550 eV. The interaction between ions and valence electrons was described by the projector augmented wave method (PAW) [50]. We have considered the GGA in the parametrization of Perdew, Burke, and Ernzerhof (PBE) [51] for the description of the exchange correlation function. Since the standard band theory (GGA) cannot describe strongly correlated d electrons with sufficient accuracy, we have considered the contribution of Hubbard parameter U as GGA+U to correctly describe the strong on-site Coulomb interaction of localized electrons. The implementation of GGA+U was achieved according to Dudarev's approach [52], where the on-site Coulomb interaction and exchange are considered through an effective parameter $U_{\mathrm{eff}} = U–J$, where U represents the Coulomb interaction and J is Hund's coupling. In our calculations, we have selected values of U and J from the calculations of Das *et al.* [29,53] obtained for the inverse spinel cobalt ferrite structure, viz., $U = 4.22$ eV and $J = 0.80$ eV are used for Fe, and $U = 4.08$ eV and $J = 0.79$ eV for Co, for normal and inverse spinel cobalt ferrite structures [54].

Fritsch *et al.* investigated different possible cation distributions on the spinel B-site sublattice for cobalt and nickel ferrite [55,56]. It was demonstrated that the specific cation distribution on the sublattices leads to an artificially lowered symmetry [55,56]. Hence for CF1, the unit cell we considered includes eight formula unit cells, i.e., 56 atoms, to preserve the highest possible symmetry. The structure consists of the cubic system of space group $Fd3m$ (227). The oxygen atoms occupy 32e positions, tetrahedral Fe occupies the 8a position, and the octahedral Co and octahedral Fe atoms are distributed equally on 16d positions. The unit cell consists of 24 magnetic atoms. For a CF2 structure, we used a $2 \times 1 \times 1$ supercell of CF1 structure leading to 112 atoms system. Within the ideal inverse spinel distribution, it can be expressed as $(\mathrm{Fe}_{16})_{\mathrm{Tet}}(\mathrm{Co}_{16}\mathrm{Fe}_{16})_{\mathrm{Oct}}\mathrm{O}_{64}$. The cation distribution we considered is a fraction of metal cations at the octahedral sites: $[(\mathrm{Co}_{1-x}\mathrm{Fe}_x)_{16}]_{\mathrm{Tet}}[(\mathrm{Co}_x\mathrm{Fe}_{2-x})_{16}]_{\mathrm{Oct}}\mathrm{O}_{64}$. For CF2 structure, we considered $x = 0.00$, 0.3125, 0.375, 0.44, 0.50, 0.56, and 1.00. In selecting the cation distribution, the atomic sites achieved maximum possible equal/homogeneous distribution so as to avoid system distortions that may occur due to clustering or segregation. The values of U and J are unchanged for Fe and Co atoms in CF1 and CF2 structure.

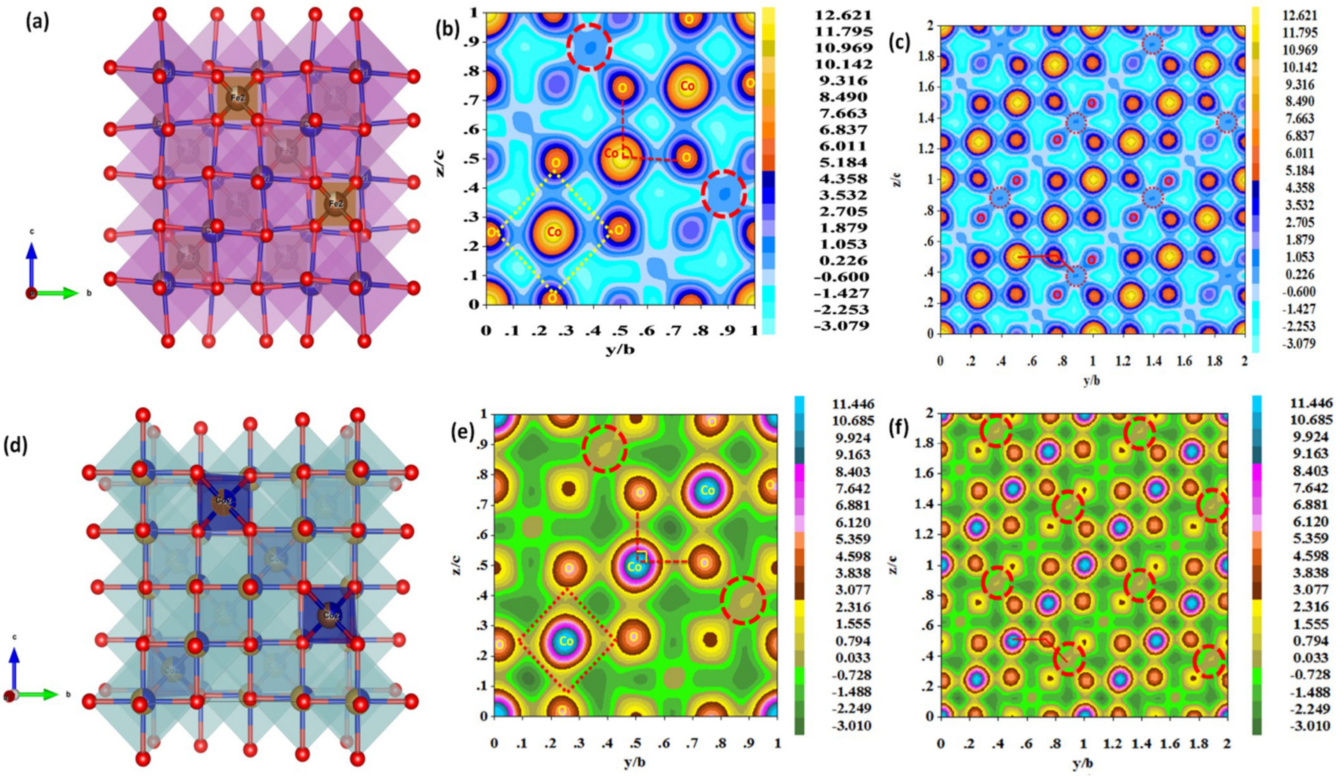

FIG. 3. The electron density (ED) plots in the yz plane taken at the $x = 0$ intercept for both CF1 (b, c) and CF2 (e, f) along with a corresponding section of the unit cell for CF1 (a) and CF2 (d).

The inverse spinel CFO structure was carefully converged for number of k points and a $7 \times 7 \times 7$ mesh of k points centered at the Γ point using a Monkhorst-Pack scheme [57], which was found suitable for normal as well as inverse, spinel unit-cell structure. We performed full geometry optimization with conserving the cell shape from first-principles calculations for CF1 and CF2 structures to find the equilibrium lattice parameters. The atomic relaxations were achieved self-consistently, with energy convergence of 10^{-7} eV, and the forces on individual atoms were reduced below 10^{-4} eV/Å. In all calculations, the magnetic moments were initiated according to the Néel configuration between the tetrahedral and octahedral sites. To compute the magnetic exchange parameters, we have calculated the total energies for ferrimagnetic and antiferromagnetic configurations, and different configurations with antiparallel moments at A and B sublattices, respectively. The magnetic inter- and intrasublattice exchange parameters are described using the classical Heisenberg Hamiltonian:

$$H_{\text{eff}} = -\sum_{i,j} \tilde{J}_{ij} \vec{S}_i \cdot \vec{S}_j = -\sum_{i,j} J_{i,j} \hat{e}_i \cdot \hat{e}_j \tag{1}$$

where J_{ij} is the magnetic exchange parameter, and $\hat{e}_i$ and $\hat{e}_j$ denote the normalized spins. To calculate all the nearest-neighbor exchange constants between sublattices A and B, the total energies of seven different spin structures for CF1 and eleven different spin configurations of CF2 structures were considered. The atom-wise nearest-neighbor information in CF1 and CF2 for ferrimagnetic (FM) and various antiferromagnetic (AFM) configurations is listed in Tables S1.1, S1.1a, S1.2, and S1.2a, respectively [58]. Their total energy differences in terms of exchange constants are indicated in Tables S1.3 and S1.4 of the Supplemental Material [58].

According to the interacting sites, the magnetic exchange interactions are classified into: J^{AA} (between A sublattices), J^{AB} (between A and B sublattices), and J^{BB} (between B sublattices). While solving simultaneous equations for J_{ij}'s as given in Tables S1.3 and S1.4 [58], we have used $S_{\text{Fe3+}} = 5/2$, $S_{\text{Co2+}} = 3/2$. Furthermore, the magnetic transition temperature T_{C} has been calculated from these magnetic exchange parameters onto the mean-field approximation (MFA) for multisublattice materials by solving a system of coupled equations [59–61]:

$$\langle e^{\mu} \rangle = \frac{2}{3k_B T_C} \sum_{\nu} J_{\mu\nu} \langle e^{\mu} \rangle \tag{2}$$

where $\langle e^{\mu} \rangle$ is the average z component of S, and the above equation (2) can be represented in the form of an eigenvalue matrix problem as

$$(\Theta - T_C \mathbf{I}) S = 0 \tag{3}$$

where $\Theta_{\mu\nu} = (2/3k_B) J_{\mu\nu}$, $\mathbf{I}$ is unit matrix, and S is a vector set of $\langle e^{\mu} \rangle$. The largest eigenvalue of matrix Θ gives the value of transition temperature T_{C}.

III. RESULTS AND DISCUSSION

A. Crystal structure

The unit-cell model [Figs. 1(a) and 1(b)] for CF1 and CF2 were designed using the VESTA software package. It is noticeable that the CF1 [Fig. 1(a)] exhibits an ideal inverse

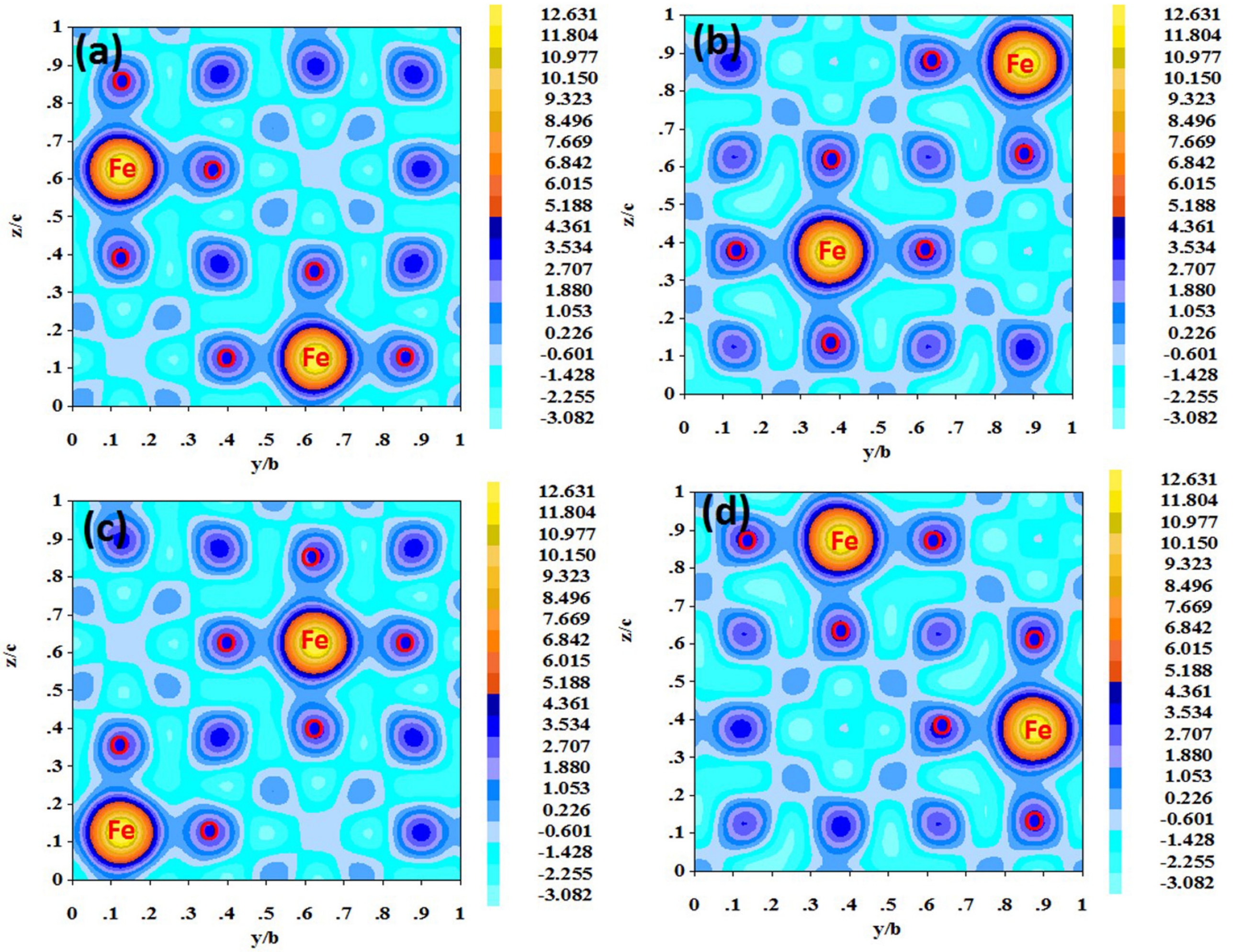

FIG. 4. The electron density (ED) plots in the yz plane taken at the x intercept of $x = 0.125$ (a), $x = 0.375$ (b), $x = 0.625$ (c), and $x = 0.875$ (d) for CF1.

cation distribution as $[\mathrm{Fe}^{+3}]_{\mathrm{Tet}}\{\mathrm{Co}^{+2}\mathrm{Fe}^{+3}\}_{\mathrm{Oct}}\mathrm{O}^{-2}{}_4$, and CF2 [Fig. 1(b)] shows a deviation from the ideal inverse cation distribution by transferring some Co^{+2} cations to the tetrahedral A site, i.e., $[\mathrm{Co}^{+2}{}_{(1-x)}\mathrm{Fe}^{+3}{}_{(x)}]_{\mathrm{Tet}}\{\mathrm{Co}^{+2}{}_{(x)}\mathrm{Fe}^{+3}{}_{(2-x)}\}_{\mathrm{Oct}}\mathrm{O}^{-2}{}_4$. Both samples are made up of a cubic close-packed array of oxygen anions occupying the 32e position. However, CF1 shows a deviation from their ideal positions, i.e., (0.25, 0.25, 0.25). The cations (Fe^{+3}, Co^{+2}, denoted as Fe1 and Co1) occupying the octahedral 16c site $\{B$ site$\}$, with a special Wyckoff position of octahedral (O_h) symmetries at (0,0,0), exhibits trigonal 3m point symmetry. The cations (Fe^{+3}, Co^{+2} denoted as Fe2 and Co2) occupying tetrahedral 8b sites [A sites], with special Wyckoff position of tetrahedral (T_d) symmetries at (5/8,5/8,5/8), exhibits cubic 43m point symmetry.

The bond lengths and bond angles obtained after full structural relaxation using DFT+U for CF1 and CF2 structures are shown in Fig. 2. The calculated lattice parameters for CF1 and CF2 structures are 8.42 and 8.48 Å, respectively. The slight local distortions at Co and Fe octahedral sites of CF1 are noted. Similarly, Fe atoms at tetrahedral sites also exhibit slight distortions, reducing the internal symmetry of the system. The calculated Fe-O and Co-O bond lengths at octahedral sites are underestimated by ∼0.2 Å, whereas the Fe-O bond length at tetrahedral sites is overestimated by ∼0.4 Å. The bond lengths and bond angles for the CF1 structure, however, agree well with the reported theoretical studies [29]. The calculated bond lengths (∼2.04 Å) at octahedral sites of CF2 structures are also distorted. The bond lengths at tetrahedral sites are calculated with an overestimation of ∼0.1 Å. Although the bond angles O-Fe-O for CF1 and CF2 at tetrahedral sites exhibit distortion; the value is close to 109°, ideal for spinel structures. The calculated $\mathrm{Fe_T}$-O-$\mathrm{Fe_O}$ angle in CF1 is ∼122°, which is underestimated from the ideal spinel value of 125°, and this result agrees well with the previous theoretical results by Das *et al.* [29]. The $\mathrm{Fe_T}$-O-$\mathrm{Fe_O}$ angle is also calculated to be 122° for the CF2 structure. The O-Fe-O angle calculated at the octahedral sites measures large deviation up to 3° in CF1, whereas it is up to 4.8° in the CF2 structure, rather than the ideal spinel value of 90°.

The distortion observed due to the particle-size reduction is further explained using the electron density (ED) maps. For the sake of simplicity, only the yz plane of interest with various appropriate intercepts are plotted as shown in Fig. 3 for CF1 and CF2. The ED maps play a significant role in understanding the interactions at the atomic level. The first

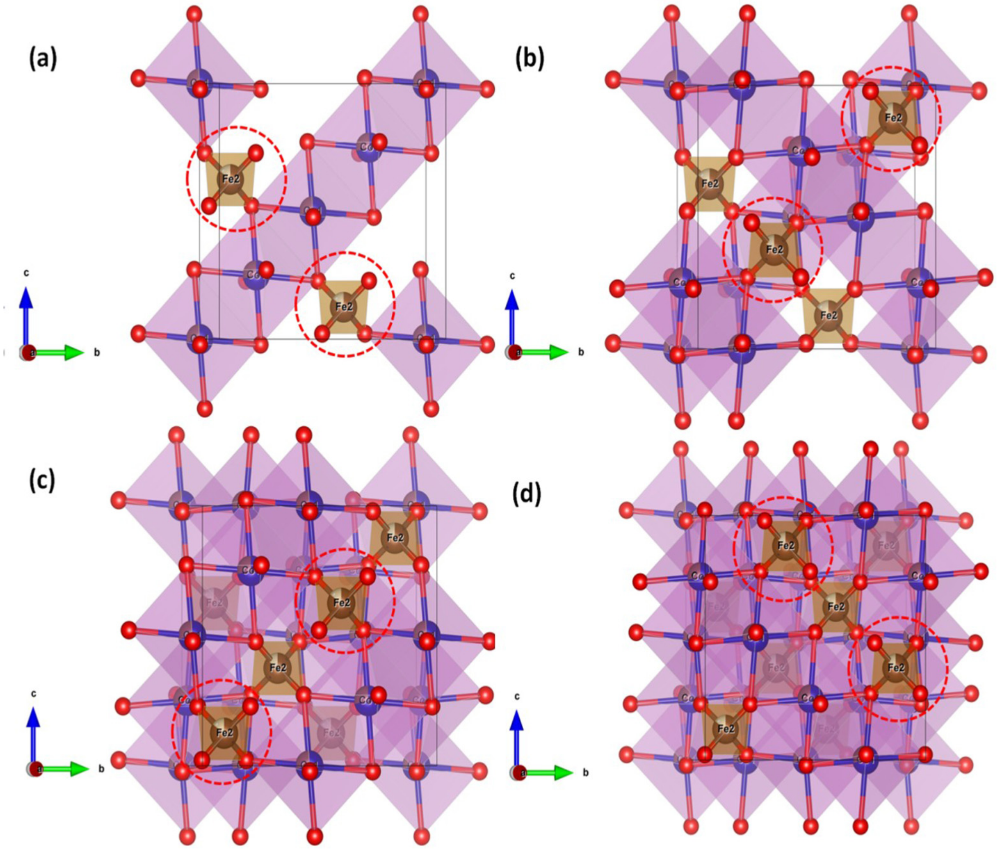

FIG. 5. The unit cell of CF1 in the yz plane, taken at an x intercept of $x = 0.125$ (a), $x = 0.375$ (b), $x = 0.625$ (c), and $x = 0.875$ (d) for clarification.

row in Fig. 3 shows the ED on the yz plane, taken at the y intercept of zero for CF1, and similar data is shown for the CF2 sample in the second row. In the present study, for CF1 and CF2, different sublattice occupancy may be due to the "inverted" structure that introduces the qualitative differences of the electron density map at both the tetrahedral (A) and octahedral (B) sites. In the left column of Figs. 3(a) and 3(d), the corresponding section of the unit cell is shown. In row 1, the sections are taken such that the electron density in the yz plane of FeO_6 and CoO_6 octahedra is evident. The interactions between the cation, i.e., Co1, Fe1, and O^{-2} anions within a octahedral site are evident in the yz plane at $x = 0$. In this plane, the Co1–O bonds are visible and appear to form a cube comprised of Co1 or Fe1 atom at the center and oxygen atoms at the vertices (red and yellow solid cubic drawn as a guide to eye). Here, electron clouds of d orbital cations are higher than the anion (O^{-2}) cloud due to the higher atomic number of cations compared to oxygen. Importantly, in the yz plane, a diagonally arranged perfect cube of oxygen does not deviate from a perfect cube as the particle size is reduced to $\approx$20 nm (CF1), although the Co1–O bond length increases as discussed above. However, a small electron density anisotropy is seen for CF1 compared to CF2 as the O–Co–O bond angle deviates from the ideal value of CF1. It is evident from the electron density map that CF2 slightly deviates from the ideal inverse spinel structure as the electron cloud density observed at the octahedral site for CF1 is slightly high compared to the electron cloud density observed for CF2 at the octahedral site. Furthermore, it is evident from Fig. 3 that the octahedral and tetrahedral sites have slightly different electron density distributions for CF1 and CF2, as marked by the red circle in Figs. 3(b), 3(c), 3(e), and 3(f). Further insights into electron density distributions are derived by means of the ED maps are shown in Figs. 4–6. In order to get a deeper insight into the ED within a tetrahedral site, the ED maps in the yz plane, taken at an x intercepts of 0.125, 0.375, 0.625, and 0.875 for CF1 and CF2, are illustrated in Figs. 4 and 6, respectively. The corresponding section of the unit cell is shown in Figs. 5 and 7 for CF1 and CF2, respectively. This further supports our prediction about the ideal and deviated inverse spinel cation distribution for CF1 and CF2, respectively. From Figs. 3(c) and 3(f), we have observed that the bond angles Co1–O–Fe2 and Fe1–O–Fe2 are 131.64°, and for CF1 there is a larger deviation from the ideal spinel value of 125°. It is also noted, for CF1, that the shape of the electron density around Fe1 or Co1 is slightly anisotropic. This investigation of two different particle sizes of CFO further adds to our understanding of the observed changes in magnetic properties of CF1 and CF2. This result can indirectly explain why composition variation in CFO tends to show different physicochemical properties despite the similar structural arrangement. Furthermore, the difference in the band structure can be envisioned for different CFO compositions, indicating its intrinsic correlation with magnetism in these materials.

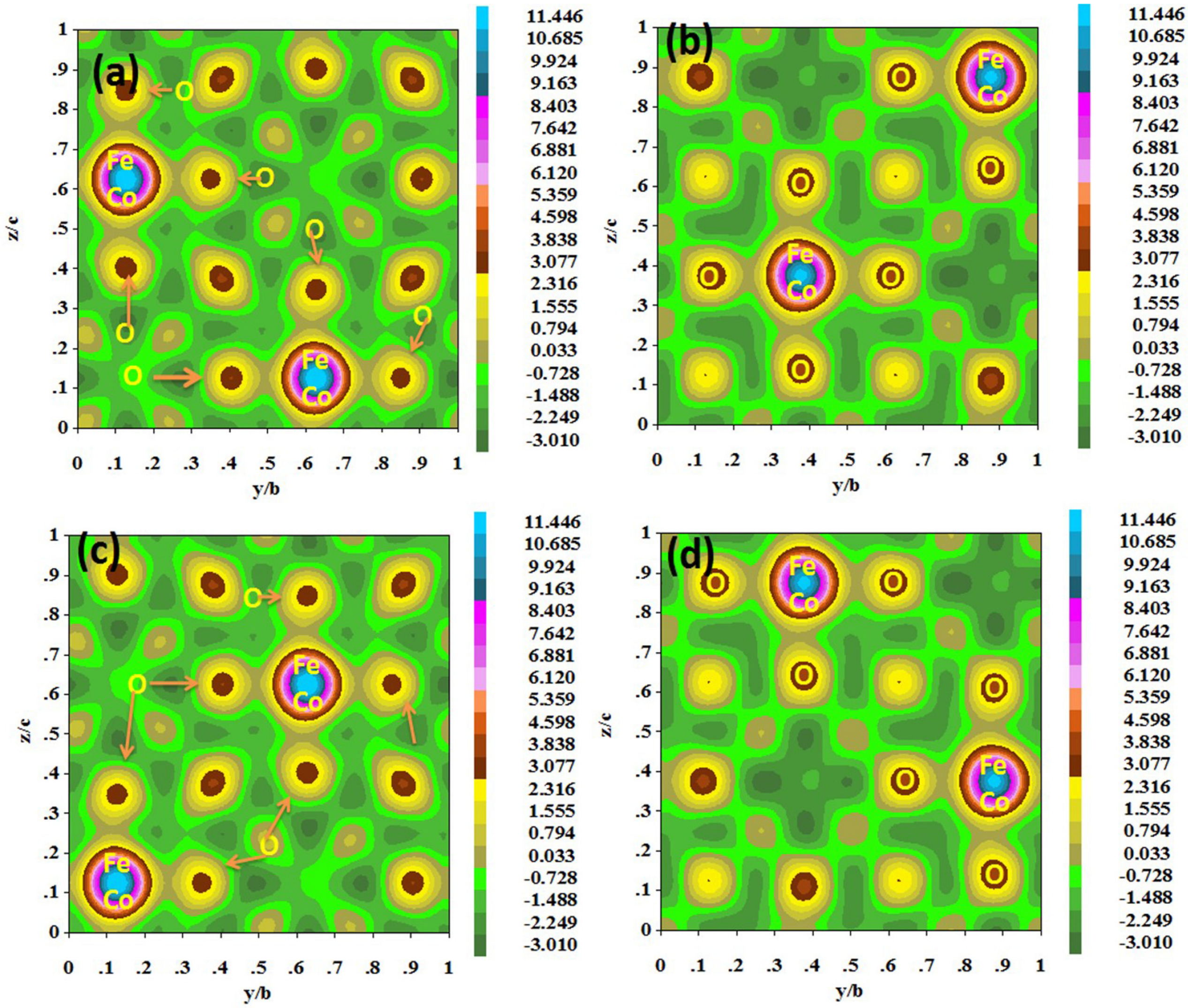

FIG. 6. The electron density (ED) plots in the yz plane taken at the x intercept of $x = 0.125$ (a), $x = 0.375$ (b), $x = 0.625$ (c), and $x = 0.875$ (d) for CF2.

B. Electronic structure and magnetic moments

It is well known that the configurations of d electrons at different cation sites play the most important role in determining the electronic and magnetic properties of spinel oxides. According to crystal-field theory [62], the electronic configuration depends on the relative strengths of the crystal-field (CF) and intra-atomic exchange field (EX). In this section, we attempt to understand the relation between structural distortions and electronic structures in CF1 and CF2 by investigating the relative strengths of CF splitting and EX splitting through an analysis of the densities of states (DOS). Consequently, this would lead to the understanding of electronic and magnetic properties of CF1 and CF2 appropriately. The spin configurations of inverse $[\mathrm{Co}^{+2}{}_{(1-x)}\mathrm{Fe}^{+3}{}_{(x)}]_{\mathrm{Tet}}\{\mathrm{Co}^{+2}{}_{(x)}\mathrm{Fe}^{+3}{}_{(2-x)}\}_{\mathrm{Oct}}\mathrm{O}^{-2}$ spinel structures with $x = 0.31$, 0.38, 0.44, 0.50, 0.56, and 1.00 are considered and investigated to illustrate the nature of magnetic properties of CF1 and CF2 samples. The $\mathrm{Fe}^{+3}(d^5)$ and $\mathrm{Co}^{+2}(d^7)$ cations possess different local symmetries at different lattice sites. According to the CF theory, the e_g levels are lower than the t_{2g} levels in a tetrahedral CF due to the direct electrostatic repulsion between the d_{xy}, d_{yz}, and d_{zx} orbitals and surrounding anion orbitals, while the order is reversed in the octahedral environment as the $d_z{}^2$ and $d_{x^2\_y^2}$ orbitals are repelled directly. The electronic configuration depends on the relative strength of CF and EX values, which results in possible high-spin (CF<EX) or low-spin (CF>EX) configurations [62]. In the present study, the schematic representation of electrons in d levels based upon crystal-field theory for CF1 and CF2 is shown in Fig. S1 (Supplemental Material [58]).

We have investigated the effect of change in sublattice occupancy, in the inverted structure, on the electronic density of states (DOS) at both the tetrahedral and octahedral sites as shown in Figs. 8(a) and 8(b). The upper panel of either plots indicate the total density of states calculated in the unit cell. The electronic structure calculated without consideration of strong correlation exhibit metallic behavior (not shown here). The application of Hubbard U, as explained in the computational details, introduces large EX splitting leading to the semiconducting nature. In the CF1 structure [Fig. 8(a)],

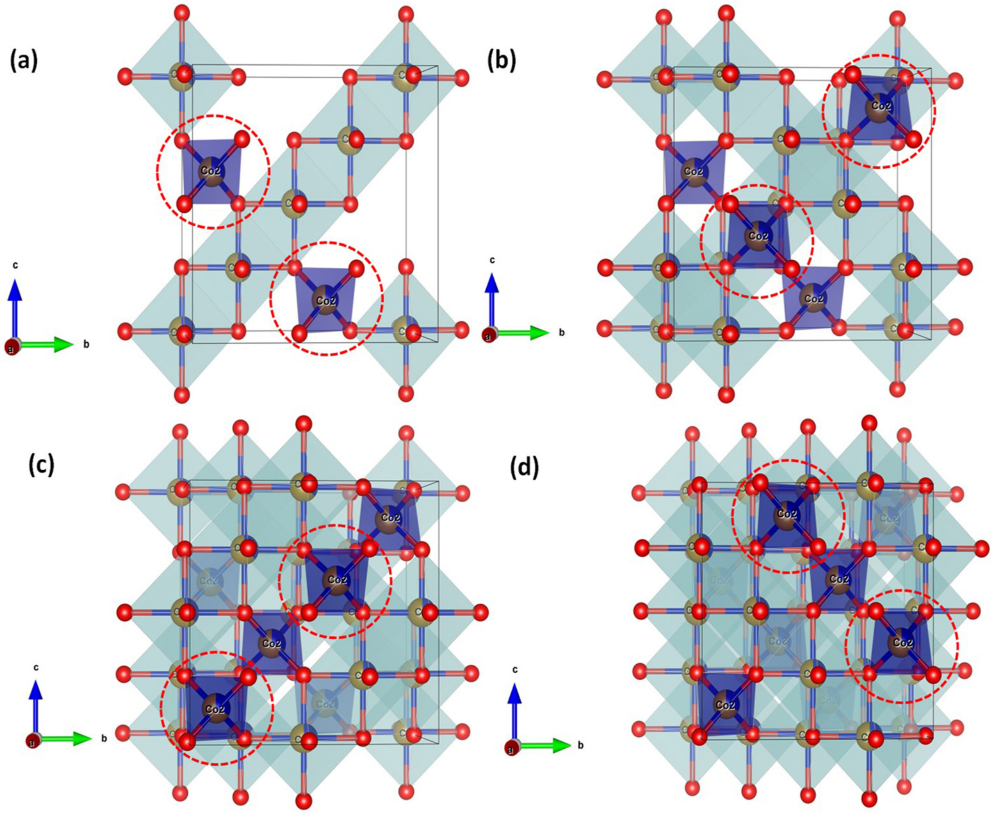

FIG. 7. The unit cell of CF2 in the yz plane, taken at the x intercept of $x = 0.125$ (a), $x = 0.375$ (b), $x = 0.625$ (c), and $x = 0.875$ (d) for clarification.

the tetrahedral sites are occupied by Fe^{+3} ions, which exhibit strongly localized e_g and t_{2g} states. The $e^{\uparrow}{}_g$ and $t^{\uparrow}{}_{2g}$ states of Fe^{+3} ions at sublattice A are completely empty and lie around 2 eV above the Fermi energy. The $e^{\downarrow}{}_g$ and $t^{\downarrow}{}_{2g}$ Fe states at sublattice A are situated deep below the Fermi energy (-5 to -6 eV). The octahedral sites are occupied by both the Fe^{+3} and Co^{+2} ions. The e_g and t_{2g} states for Fe^{+3} at the octahedral site show a completely opposite nature than that for the tetrahedral site. The unoccupied $e^{\downarrow}{}_g$ states of Fe^{+3} at octahedral sites are situated at higher energy than t_{2g} states, whereas this order is reversed at the tetrahedral sites. However, the e_g and t_{2g} states of Fe^{+3} show highly localized character irrespective of sublattice occupancy. In comparison with Fe^{+3} states, Co^{+2} states are relatively delocalized, especially for majority spin states. The spin minority d_{xz} and d_{yz} states of Co^{+2} contribute near the Fermi energy at around -0.5 eV. The e_g degeneracy is not broken completely at sublattice B due to the absence of $e^{\downarrow}{}_g$ states. The O-2p states are seen to hybridize with the delocalized t_{2g} states of Co^{+2}. The magnetic moments for Fe atoms at tetrahedral sites are observed to be 3.98 μ_{B}, whereas the magnetic moments for Fe and Co at octahedral sites are 4.09 and 2.60 μ_{B}, respectively. The ground-state magnetic structure of CF1 lattice is of ferromagnetic Néel type, where the magnetic moments at sublattices A and B align in opposite directions. Thus, the total magnetic moment is calculated to be 3.0 μ_{B}/F.U. for CF1, which is in agreement with those reported in the literature [28,29].

Unlike the CF1 structure, CF2 has Fe as well as Co atoms at the tetrahedral site. This is due to some of the Co^{+2} ions moving from the octahedral to tetrahedral site. This movement of ions changes the total magnetic moment of the unit cell. We performed the calculations for various x values, $x = 0.0$, 0.3125, 0.38, 0.44, 0.50, 0.56, and 1.00 (see Table I). To gain further insights and to probe the magnetic properties, we have investigated the detailed electronic structure and calculations made ($x = 0.3125$) [63]. The electronic DOS is plotted and shown in Fig. 8(b). In the CF2 structure, Co atoms break t_{2g} degeneracy at octahedral as well as tetrahedral sites. In particular, the $e^{\downarrow}{}_g$ and $t^{\downarrow}{}_{2g}$ states of Co at tetrahedral sites are completely occupied and located well below the Fermi energy. The Fe-d minority spin states are delocalized and hybridize with O-2p states along with Co t_{2g} states. The majority spin states of Fe and Co are highly localized, with Co e_g states being completely filled. At octahedral sites, the states near the Fermi energy are mainly due to e_g and t_{2g} states of Co atoms. The $e^{\uparrow}{}_g$ and $t^{\uparrow}{}_{2g}$ states are completely filled at A and B sublattices. The $t^{\downarrow}{}_{2g}$ for Co atoms appears near the Fermi energy at around -1 eV, whereas all Fe d states are unfilled. A comparative study of the electronic structure reveals that the Co states are delocalized irrespective of the crystal environment, whereas Fe states are localized in CF1 and CF2. This influences the magnetic exchange interaction that is explicitly discussed in the present work. The calculated magnetic moment of Fe and Co atoms at tetrahedral sites are 3.95 and 2.47μ_{B}, respectively. These values are also retained for other higher x values. At octahedral sites, the calculated magnetic moments for Fe and Co atoms are 4.12 and 2.67 μ_{B}, respectively. As the degree of inversion parameter x is

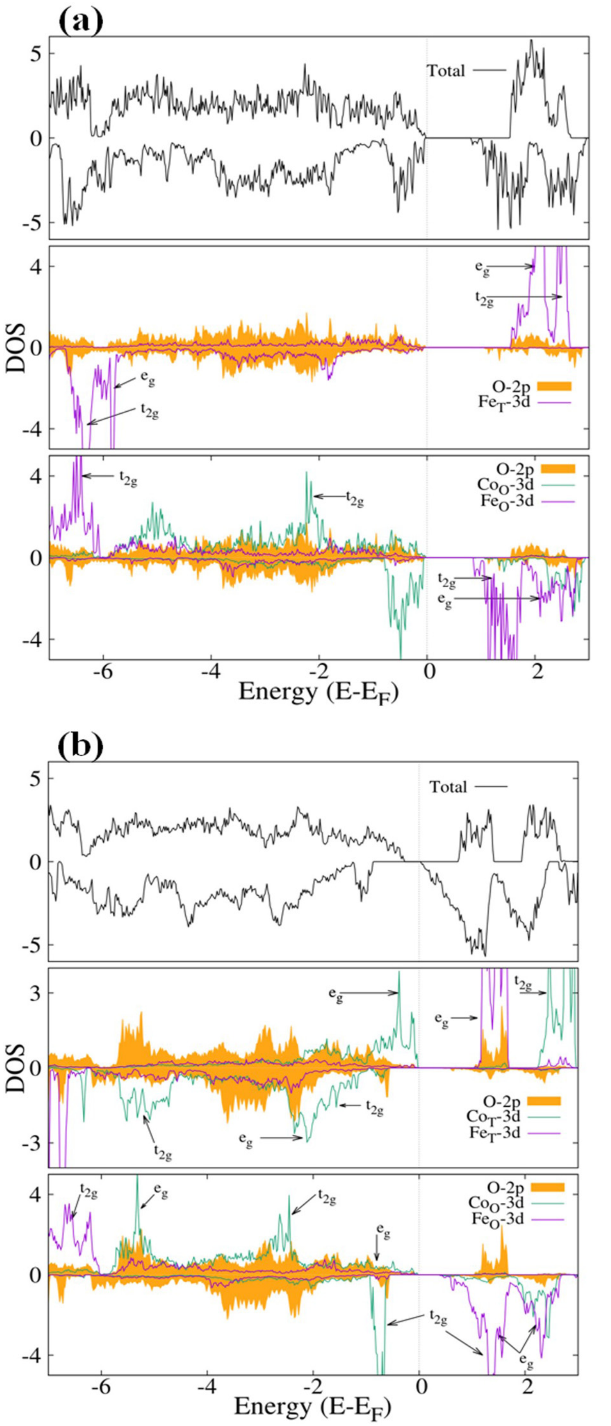

FIG. 8. The site-projected density of states for CF1 (a) and CF2 (b), where identified tetrahedral and octahedral density of states are shown in the middle and bottom panel, whereas the upper panel indicates the total density of states.

increased from 0.31 to 0.56, the magnetic moment of Co is slightly reduced from 2.67 to 2.63 μ_B, whereas the moment on Fe atoms remain unaffected. The calculated total magnetic moment for the CF2 structure is 5.73 μ_B/F.U.

TABLE I. The calculated magnetic moments in a Bohr magneton for A (μ_A), B (μ_B) cations and the total magnetic moment (μ_T) per formula unit, where the (+/−) signs are according to the global spin axis of the inverse spinel structure.

Sample	A site	μ_A	B site	μ_B	μ_T
CF1	Fe$_T$	−3.98	Fe$_O$	4.09	**3.0**
$x = 1.0$			Co$_O$	2.60	
CF2	Fe$_T$	−3.95	Fe$_O$	4.12	**5.73**
$x = 0.3125$	Co$_T$	−2.47	Co$_O$	2.67	
CF2	Fe$_T$	−3.97	Fe$_O$	4.13	5.44
$x = 0.375$	Co$_T$	−2.47	Co$_O$	2.64	
CF2	Fe$_T$	−3.97	Fe$_O$	4.13	5.13
$x = 0.44$	Co$_T$	−2.47	Co$_O$	2.66	
CF2	Fe$_T$	−3.97	Fe$_O$	4.13	5.00
$x = 0.50$	Co$_T$	−2.47	Co$_O$	2.63	
CF2	Fe$_T$	−3.94	Fe$_O$	4.12	4.73
$x = 0.56$	Co$_T$	−2.47	Co$_O$	2.63	

Table II represents the exchange field splitting (Δ_{EX}) calculated for CF1 and CF2 along with various values of x. Table III presents the crystal-field splitting (Δ_{CF}) calculated for CF1 and CF2. For the EX splitting as well the CF splitting, the calculations were performed without considering the electron correlations, i.e., $U_{\text{eff}} = 0$ is set in all the respective calculations. It can be observed from Table II that the magnitudes of EX splitting for e_g and t_{2g} states are competitive, irrespective of the crystal environment in CF1 and all CF2 structures. The Fe^{+3} occupying tetrahedral sites in CF1 has two electrons less than that of Co^{+2}, making the $e^{\uparrow}{}_g$ state completely empty. At the tetrahedral site, both the $e^{\uparrow}{}_g$ and $t^{\uparrow}{}_{2g}$ states are empty; however, the $t^{\uparrow}{}_{2g}$ states are higher in energy compared to $e^{\uparrow}{}_g$. Due to two extra electrons for Co^{+2}, the $t^{\uparrow}{}_{2g}$ states at octahedral sites are completely filled and located at −2.5 eV below the Fermi energy. The $e^{\downarrow}{}_g$ states of Co^{+2} at octahedral sites are completely filled, whereas the $t^{\downarrow}{}_{2g}$ are empty. In general, the EX splitting for Fe is larger than Co irrespective of the crystal environment due to the fact that Fe has one spin channel completely full, whereas due to more electrons in Co than Fe, the another spin channel in Co is also partly occupied, leading to reduced spin imbalance than Fe atoms. Unlike in CF1 structure, tetrahedral sites in the CF2 structure are partly occupied by Co atoms. The magnitude of EX splitting for

TABLE II. Exchange splitting (Δ_{EX}) results for CF1 and CF2.

	At tetrahedral site			At octahedral site		
Sample	Ion	$\Delta_{EX}^{e_g}$	$\Delta_{EX}^{t_{2g}}$	Ion	$\Delta_{EX}^{e_g}$	$\Delta_{EX}^{t_{2g}}$
CF1	Fe^{3+}	3.3	3.13	Fe^{3+}	3.5	3.36
				Co^{2+}	3.04	2.31
CF2	Fe^{3+}	3.51	3.17	Fe^{3+}	3.55	3.49
$x = 0.3125$	Co^{2+}	2.74	2.70	Co^{2+}	3.03	2.23
CF2	Fe^{3+}	3.51	3.13	Fe^{3+}	3.53	3.32
$x = 0.375$	Co^{2+}	2.64	2.71	Co^{2+}	2.89	2.15
CF2	Fe^{3+}	3.52	3.12	Fe^{3+}	3.37	3.39
$x = 0.44$	Co^{2+}	2.68	2.70	Co^{2+}	2.64	2.25
CF2	Fe^{3+}	3.31	3.13	Fe^{3+}	3.29	3.40
$x = 0.50$	Co^{2+}	2.61	2.75	Co^{2+}	2.33	2.80
CF2	Fe^{3+}	3.32	3.41	Fe^{3+}	3.47	3.44
$x = 0.56$	Co^{2+}	2.60	2.70	Co^{2+}	0.30	0.40

TABLE III. Crystal-field splitting (Δ_{CF}) results for CF1 and CF2.

	At tetrahedral site			At octahedral site		
Sample	Ion	$\Delta^{\uparrow}_{\mathrm{CF}}$	$\Delta^{\downarrow}_{\mathrm{CF}}$	Ion	$\Delta^{\uparrow}_{\mathrm{CF}}$	$\Delta^{\downarrow}_{\mathrm{CF}}$
CF1	Fe^{3+}	0.70	1.07	Fe^{3+}	1.92	1.60
				Co^{2+}	1.80	1.94
CF2 $x = 0.3125$	Fe^{3+}	0.63	0.76	Fe^{3+}	1.52	1.47
	Co^{2+}	0.90	0.57	Co^{2+}	0.87	1.92

Fe atoms is hardly affected for all other CF2 structures and is independent of the crystal environment. However, the EX splitting is more reduced for Co atoms at the tetrahedral site of the CF2 structure than that for the octahedral site. This is due to the change in hybridization with the oxygen atoms in the tetrahedral ambience.

The CF splitting values (Table III) are significantly smaller in magnitude than the EX splitting (Table II) for Fe as well as Co atoms in all the structures. Overall, the CF splitting at tetrahedral sites is lower than that for octahedral sites, irrespective of the spin channel and choice of the chemical element. At the tetrahedral site, the CF splitting is smaller for majority states than the minority states, whereas this scenario is opposite for atoms at the octahedral site. With the increase of Co^{+2} content at the tetrahedral site, the CF is reduced significantly irrespective of the spin type and sublattice A or B. The origin behind the reduced CF splitting lies in the electronic configuration of e_g and t_{2g} states for Fe^{+3} and Co^{+2} cations at A and B sites. Due to the competition of CF splitting and EX splitting, the ground-state properties of CF1 and CF2 structures are strongly influenced. The weaker CF splitting in comparison with EX splitting results in reducing the band gap. From the Tables II and III, it can be revealed that as the degree of inversion x is increased in CF2 structure, the EX splitting is barely affected, but the CF splitting is significantly reduced. This results in a more decreased band gap in the CF2 structure up to 0.3 eV than that of 0.8 eV for the CF1 structure. The EX for Co^{+2} t_{2g} states at tetrahedral sites remains unaffected, and the values are around 2.70 eV.

C. Magnetic exchange interactions

The magnetic exchange interactions are computed in terms of the classical Heisenberg Hamiltonian [Eq. (1)] for intra- and intersublattices A and B, respectively. The calculated values are listed in Table IV. The calculations were performed by considering only the nearest-neighbor sublattice interactions, as the contribution of higher-order neighboring sites in the total magnetic exchange energy is negligible. It can be seen from Table IV that, for CF1 structure, $J_{\mathrm{AB}}/J_{\mathrm{AA}} = 11.05$ and $J_{\mathrm{AB}}/J_{\mathrm{BB}} = 2.20$–$9.98$, indicating that the interlattice $A - B$ interactions are dominant over intrasublattice interactions (AA and BB). This favors collinear alignment of spins in CFO, within the ferromagnetic Néel configuration, due to the sign and strength of the dominant exchange J_{AB}. The reason behind this strong antiferromagnetic A-B interaction is that the A-site t_{2g} orbitals and B-site e_g orbitals (for both Fe and Co at the B site) are half-filled. The dominant J_{AB} interaction over J_{AA} and J_{BB} is qualitatively in good agreement with the previous results [29]. We extended the treatment to compute the magnetic exchange parameters to the partially inverse spinel structure. It can be observed from Table IV that, similar to the CF1 structure, the CF2 structure also exhibits a dominant interlattice exchange interaction J_{AB}. Due to the accessibility of tetrahedral sites for a few Co atoms (i.e., because of change in the inversion parameter x), different types of J_{AB} exchange interactions are introduced, as shown in Table IV. The Fe atoms at the tetrahedral sites do not have the nearest-neighbor Fe atoms, since all neighboring sites are occupied by Co atoms during the inversion of x. Hence compared with CF1, the magnetic exchange interactions in CF2 structure show enhanced magnitude. Interestingly, $J_{\mathrm{Co-Co}}$ exhibits dominant exchange interaction in the CF2 structure; however, overall $J_{\mathrm{AB}} > J_{\mathrm{BB}} > J_{\mathrm{AA}}$, indicating collinear magnetic stability. Our calculated value of the magnetic transition temperature, using the mean-field approximation according to Eq. (3), for CF1 is 480 K. The estimated value of magnetic transition temperature in CF2 structure is smaller (226 K) than the ideal inverse spinel CF1 structure.

IV. SUMMARY AND CONCLUSIONS

We have performed a systematic investigation of the structural and magnetic properties for inverse spinel CFO nanoparticles and nanostructured CFO microgranules using first-principles density functional theory and the electron density maps. The understanding of properties of these compounds is performed by quantifying the relative strengths of the CF effect and the exchange effect through an analysis of their electronic structure. We conclude that the electron–electron interactions of the magnetic cations play a very important role, and without the incorporation of this, the correct ground-state structures cannot be obtained. The electronic structures of these compounds are significantly different, as the cation

TABLE IV. The magnetic exchange parameters (J_{ij} in meV) and the ferrimagnetic transition temperatures (T_c in K) for CF1 and CF2.

Sample	Type of *AA* pair	J_{AA}	Type of *BB* pair	J_{BB}	Type of *AB* pair	J_{AB}	T_C (K)
CF1	$\mathrm{Fe_T}$–$\mathrm{Fe_T}$	−0.65	$\mathrm{Co_O}$–$\mathrm{Co_O}$	−3.27	$\mathrm{Fe_T}$–$\mathrm{Co_O}$	−7.18	480
$x = 1$			$\mathrm{Fe_O}$–$\mathrm{Fe_O}$	−1.93	$\mathrm{Fe_T}$–$\mathrm{Fe_O}$	−6.60	
			$\mathrm{Fe_O}$–$\mathrm{Co_O}$	0.72	–	–	
CF2	$\mathrm{Fe_T}$–$\mathrm{Fe_T}$	0.00	$\mathrm{Co_O}$–$\mathrm{Co_O}$	−13.40	$\mathrm{Fe_T}$–$\mathrm{Co_O}$	−8.27	226
$x = 0.3125$	$\mathrm{Co_T}$–$\mathrm{Co_T}$	−0.44	$\mathrm{Fe_O}$–$\mathrm{Fe_O}$	−1.26	$\mathrm{Fe_T}$–$\mathrm{Fe_O}$	−6.09	
	$\mathrm{Fe_T}$–$\mathrm{Co_T}$	−1.51	$\mathrm{Fe_O}$–$\mathrm{Co_O}$	−0.06	$\mathrm{Co_T}$–$\mathrm{Co_O}$	−4.01	
	–	–	–	–	$\mathrm{Co_T}$–$\mathrm{Fe_O}$	−6.07	

distribution changes among the tetrahedral and octahedral sites, and also the crystallite size is changed. This, in turn, affects the interatomic magnetic exchange interactions considerably and is responsible for different spin structures of these systems. In this work, understanding of the trends in the magnetic properties are attempted through proper quantification of the associated quantities and by providing necessary explanations from the trends in the local structural parameters and the electronic structures. Our results show that both the CFO nanoparticles and nanostructured CFO microgranules energetically favor inverse spinel structure, and in each case Fe and Co always prefer a high-spin configuration, no matter whether they are in octahedral or tetrahedral sites in the partial inverse spinels. As the degree of inversion (x) increases, the total magnetic moment of CFO increases. The lattice parameter of the spinel increases slightly with increasing inversion parameter x. The Co ions in the partial inverse spinel favor being far away from each other, allowing a reasonable study of the system with relatively small unit cells.

ACKNOWLEDGMENTS

S.M.A. gratefully acknowledges the financial support from Bhabha Atomic Research Centre (BARC), Mumbai, for the award of a Senior Research Fellowship under a Bhabha Atomic Research Centre (BARC) UoP memorandum (Grant Code GOI–E-175). C.V.R. acknowledges with pleasure support from the National Science Foundation (NSF), USA, with NSF-PREM Grant No. DMR-1827745. V.K. gratefully acknowledges the computational resources, viz., iff003 cluster, at Forschungszentrum Jülich. The authors thank and acknowledge special assistance from Prof. Dr. Arturo Bronson, especially for all the technical discussions, feedback, and insightful comments to improve the technical merit and presentation style.

[1] S. Gyergyek, D. Makovec, A. Kodre, I. Arčon, M. Jagodič, and M. Drofenik, J. Nanoparticle Research **12**, 1263 (2010).

[2] J. G. Na, T. D. Lee, and S. J. Park, J. Mater. Sci. Lett. **12**, 961 (1993).

[3] H. S. C. O'Neill, M. James, W. A. Dollase, and S. A. T. Redfern, Eur. J. Mineral. **17**, 581 (2005).

[4] P. F. Ndione, Y. Shi, V. Stevanovic, S. Lany, A. Zakutayev, P. A. Parilla, J. D. Perkins, J. J. Berry, D. S. Ginley, and M. F. Toney, Adv. Funct. Mater. **24**, 610 (2014).

[5] J. M. Hastings and L. M. Corliss, Phys. Rev. **104**, 328 (1956).

[6] E. L. Uzunova, I. G. Mitov, and D. G. Klissurski, Bull. Chem. Soc. Japan. **70**, 1985 (1997).

[7] T. A. S. Ferreira, J. C. Waerenborgh, M. H. R. M. Mendonca, M. R. Nunes, and F. M. Costa, Solid State Sci. **5**, 383 (2003).

[8] B. P. Urubega, D. D. Barcorisen, R. Smith, J. A. Ball, R. W. Grimes, A. F. Voter, and K. E. Sickafus, Phys. Rev. B **75**, 104116 (2007).

[9] K. E. Sickafus, J. Nucl. Mater. **219**, 128 (1995).

[10] L. Schwarz, Z. Galazka, T. M. Gesing, and D. Klimm, Cryst. Res. Technol. **50**, 961 (2015).

[11] S.-H. Lee, C. Broholsm, T. H. Kim, W. Ratcliff II, and S.-W. Cheong, Phys. Rev. Lett. **84**, 3718 (2000).

[12] J. H. Chung, M. Matsuda, S. H. Lee, K. Kakurai, H. Ueda, T. J. Sato, H. Takagi, K. P. Hong, and S. P. Park, Phys. Rev. Lett. **95**, 247204 (2005).

[13] K. Hasz and Y. Ijiri, Phys. Rev. B. **90**, 180405(R) (2014).

[14] P. A. Kumar, S. Ray, S. Charkraverty, and D. D. Sarma, Appl. Phys. Lett. **103**, 102406 (2013).

[15] H. Shenker, Phys. Rev. **107**, 1246 (1957).

[16] R. H. Kodama, A. E. Berkowitz, E. J. Mc Niff, and S. Foner, Phys. Rev. Lett. **77**, 394 (1996).

[17] D. A. Garanin and H. Kachkachi, Phys. Rev. Lett. **90**, 065504 (2003).

[18] V. Skumryev, S. Stoyanov, Y. Zhang, G. Hadjipanayis, D. Givord, and J. Nogues, Nature (London) **423**, 850 (2003).

[19] J. C. Slonczewski, Phys. Rev. **110**, 1341 (1958).

[20] L. Braicovich, A. Tagliaferri, G. van der Laan, G. Ghiringhelli, and N. B. Brookes, Phys. Rev. Lett. **90**, 117401 (2003).

[21] J. A. Moyer, C. A. F. Vaz, D. A. Arena, D. Kumah, E. Negusse, and V. E. Henrich, Phys. Rev. B. **84**, 054447 (2011).

[22] J. Kanamori, in *Magnetism* (Academic Press, New York, 1963).

[23] M. Penicaud, B. Siberchicot, C. B. Sommer´s, and J. Kubler, J. Magn. Magn. Mater. **103**, 212 (1992).

[24] V. N. Antonov, B. N. Harmon, and A. N. Yaresko, Phys. Rev. B. **67**, 024417 (2003).

[25] A. Walsh, S. H. Wei, Y. Yan, M. M. Al-Jassim, and J. A. Turner, M. Woodhouse, and B. A. Parkinson, Phys. Rev. B. **76**, 165119 (2007).

[26] Z. Szotek, W. M. Temmerman, D. Kodderitzsch, A. Svane, L. Petit, and H. Winter, Phys. Rev. B. **74**, 174431 (2006).

[27] N. M. Caffrey, D. Fritsch, T. Archer, S. Sanvito, and C. Ederer, Phys. Rev. B **87**, 024419 (2013).

[28] Y. H. Hou, Y. J. Zhao, Z. W. Liu, H. Y. Yu, X. C. Zhong, W. Q. Qiu, D. C. Zeng, and L. S. Wen, J. Phys. D: Appl. Phys. **43**, 445003 (2010).

[29] D. Das, R. Biswas, and S. Ghosh, J. Phys.: Condens. Matter. **28**, 446001 (2016).

[30] W. M. Temmerman, A. Svane, Z. Szotek, and H. Winter, *Electronic Density Functional Theory: Recent Progress and New Directions* (Plenum, New York, 1998).

[31] D. Fritsch and C. Ederer, Appl. Phys. Lett. **99**, 081916 (2011).

[32] A. Aubert, V. Loyau, Y. Pascal, F. Mazaleyrat, and M. LoBue, Phys. Rev. Appl. **9**, 044035 (2018).

[33] G. Lavorato, E. Winkler, A. Ghirri, E. Lima, D. Peddis, H. E. Troiani, D. Fiorani, E. Agostinelli, D. Rinaldi, and R. D. Zysler, Phys. Rev. B **94**, 054432 (2016).

[34] G. Lavorato and E. Winkler, B. Rivas-Murias, and F. Rivadulla, Phys. Rev. B **94**, 054405 (2016).

[35] M. Valvidares, N. Dix, M. Isasa, K. Ollefs, F. Wilhelm, A. Rogalev, F. Sanchez, E. Pellegrin, A. Bedoya-Pinto, P. Gargiani, L. E. Hueso, F. Casanova, and J. Fontcuberta, Phys. Rev. B. **93**, 214415 (2016).

[36] M. Abes, C. T. Koops, S. B. Hrkac, J. McCord, N. O. Urs, N. Wolff, L. Kienle, W. J. Ren, L. Bouchenoire, B. M. Murphy, and O. M. Magnussen, Phys. Rev. B **93**, 195427 (2016).

[37] Z. Li, Z. Zhao, Q. Wang, and X. Yin, Mater. Res. Express **5**, 046105 (2018).
[38] J. A. Moyer, C. A. F. Vaz, E. Negusse, D. A. Arena, and V. E. Henrich, Phys. Rev. B. **83**, 035121 (2011).
[39] J. Frenkel and J. Doefman, Nature (London) **126**, 274 (1930).
[40] V. B. Gutierrez, M. R. Virumbrales, S. Puche, and J. Maria, J. Phys. Chem. C **117**, 20927 (2013).
[41] S. T. Xu, Y. Q. Ma, G. H Zheng, and Z. X. Dai, Nanoscale **7**, 6520 (2015).
[42] J. C. Fu, J. L. Zhang, Y. Peng, J. G. Zhao, G. G. Tan, N. J. Mellors, E. Q. Xie, and W. H. Han, Nanoscale **4**, 3932 (2014).
[43] L. Wu, P. O. Jubert, D. Berman, W. Imaino, A. Nelson, H. Zhu, S. Zhang, and S. Sun, Nano Lett. **14**, 3395 (2014).
[44] B. Debnath, A. Bansal, H. G. Salunke, A. Sadhu, and S. Bhattacharyya, J. Phys. Chem. C. **120**, 5523 (2016).
[45] S. Khanra, M. A. Mamun, F. F. Ferreira, K. Ghosh, and S. Guha, ACS Appl. Nano Mater. **3**, 1175 (2018).
[46] K. P. Su, C. Y. Zhao, H. O. Wang, S. Huang, Z. W. Liu, and D. X. Huo, Mater. Res. Express. **5**, 056102 (2018).
[47] G. Muscas, G. Singh, W. R. Glomm, R. Mathieu, P. A. Kumar, G. Concas, E. Agostinelli, and D. Peddis, Chem. Mater. **27**, 1982 (2015).
[48] S. M. Ansari, R. D. Bhor, K. R. Pai, S. Mazumder, D. Sen, Y. D. Kolekar, and C. V. Ramana, ACS Biomater. Sci. Eng. **2**, 2139 (2016).
[49] G. Kresse and J. Furthmüller, Comput. Mater. Sci. **6**, 15 (1996).
[50] P. E. Blöchl, Phys. Rev. B. **50**, 17953 (1994).
[51] J. P. Perdew, K. Burke, and M. Ernzerhof, Phys. Rev. Lett. **77**, 3865 (1996).
[52] S. L. Dudarev, G. A. Botton, S. Y. Savrasov, C. J. Humphreys, and A. P. Sutton, Phys Rev. B. **57**, 1505 (1998).
[53] D. Das and S. Ghosh, J. Phys. D: Appl. Phys. **48**, 425001 (2015).
[54] I. V. Solovyev, P. H. Dederichs, and V. I. Anisimov, Phys. Rev. B. **50**, 16861 (1994).
[55] D. Fritsch and C. Ederer, Phys. Rev. B. **82**, 104117 (2010).
[56] D. Fritsch and C. Ederer, Phys. Rev. B. **86**, 014406 (2012).
[57] H. J. Monkhorst and J. D. Pack, Phys. Rev. B. **13**, 5188 (1976).
[58] See Supplemental Material at http://link.aps.org/supplemental/10.1103/PhysRevB.102.035446 for additional computation details, structural information, and schematic representation of electrons in d levels based upon crystal field.
[59] E. Şaşıoğlu, L. M. Sandratskii, and P. Bruno, Phys. Rev. B. **70**, 024427 (2004).
[60] P. W. Anderson, Solid State Physics **14**, 99 (1963).
[61] Y. Kurtulus, R. Dronskowski, G. D. Samolyuk, and V. P. Antropov, Phys. Rev. B. **71**, 014425 (2005).
[62] I. B. Berusker, *Electronic Structure and Properties of Transition Metal Compounds: Introduction to the Theory* (Wiley, New York, 1996).
[63] First we performed the calculations for a wide range of x values, $x = 0.0, 0.3125, 0.38, 0.44, 0.50, 0.56$, and 1.00, with an aim to achieve reasonable agreement with the experimentally observed magnetic moment ($M_S = 5.6\mu_B$/F.U.) of the formula unit cell. The experimental data (which is not part of this manuscript) is based on our unpublished work. Based on our calculations, $x = 0.3125$ gives better agreement ($M_S = 5.73\,\mu_B$/F.U.) with the experimental value. Therefore, at $x = 0.3125$, we have investigated the detailed electronic structure calculations to probe the magnetic properties.